

# Constraint-Consistent Control of Task-Based and Kinematic RCM Constraints for Surgical Robots

Yu Li<sup>1</sup>, Hamid Sadeghian<sup>1</sup>, Zewen Yang<sup>1</sup>, Valentin Le Mesle<sup>1</sup>, and Sami Haddadin<sup>2</sup>

**Abstract**—Robotic-assisted minimally invasive surgery (RAMIS) requires precise enforcement of the remote center of motion (RCM) constraint to ensure safe tool manipulation through a trocar. Achieving this constraint under dynamic and interactive conditions remains challenging, as existing control methods either lack robustness at the torque level or do not guarantee consistent RCM constraint satisfaction. This paper proposes a constraint-consistent torque controller that treats the RCM as a rheonomic holonomic constraint and embeds it into a projection-based inverse-dynamics framework. The method unifies task-level and kinematic formulations, enabling accurate tool-tip tracking while maintaining smooth and efficient torque behavior. The controller is validated both in simulation and on a RAMIS training platform, and is benchmarked against state-of-the-art approaches. Results show improved RCM constraint satisfaction, reduced required torque, and robust performance by improving joint torque smoothness through the consistency formulation under clinically relevant scenarios, including spiral trajectories, variable insertion depths, moving trocars, and human interaction. These findings demonstrate the potential of constraint-consistent torque control to enhance safety and reliability in surgical robotics. The project page is available at <https://rcmpc-cube.github.io>

## I. Introduction

Minimally invasive surgery (MIS) reduces trauma, recovery time, and infection risk by operating through small incisions [1]. Despite these benefits, MIS remains demanding due to constrained access and safety-critical motion [2]. Robotic-assisted MIS (RAMIS) enhances dexterity and precision while reducing surgeon workload through motion scaling and tremor filtering [1], and further supports training and assessment via teleoperation and haptic feedback [3]. Central to RAMIS safety is the remote center of motion (RCM), which constrains tool motion about a trocar pivot [4]. Enforcing this constraint with high precision under dynamic and interactive conditions remains a major control challenge.

Early solutions relied on mechanical RCM mechanisms e.g., parallelogram linkages, spherical joints, and hybrid architectures [5], [6], which reliably maintain pivoting but limit adaptability and workspace flexibility. This has motivated control-based enforcement. Among these, kinematic methods incorporate constrained Jacobians [7], parameterize tool motion [8], or solve inverse kinematics and velocity control [9]. Data-driven variants



Fig. 1: Designed surgical platform or training purposes. It is composed of three Surgical Robot Manipulators (SRM): one of them is used to control an endoscope, and the two others incorporate a surgical tool drive unit, introduced in [22]. Both the drive unit and manipulators can optionally be used in a teleoperation setup.

employ recurrent models for servoing and parameter estimation [10], [11]. However, these methods are often tailored to position or velocity control and remain less compatible with torque-level implementations, where dynamic consistency and robustness are essential [12].

Implicit formulations mitigate some of these limitations. Projection-based and null-space schemes [13] implicitly enforce RCM constraints by limiting task velocities, while multi-priority control extends this idea as dynamical task constraints using augmented Jacobian [14]. In collaborative RAMIS [15], dynamic controllers further improve robustness, including disturbance compensation [16], and optimal/pассиве teleoperation frameworks [17], [18]. More recently, constrained dynamics formulations [19], [20] explicitly partition constrained and free dynamics, providing theoretical consistency. Yet these methods are often numerically fragile, computationally demanding, and limited in handling rheonomic or enforced RCM conditions arising from viscoelastic tissue motion [21].

More broadly, projected constrained dynamics and operational-space control have proven effective in contact-rich robotics [23], [24]. Orthogonal projections reduce torque effort [25], and can address friction-aware constraints through optimization-based resolutions [26], [27]. However, classical projection approaches presume rigid scleronomic constraints and remain numerically sensitive [28], [29], making them less suited to RCM constraints when the trocar is moving, and the compliance

<sup>1</sup> Munich Institute of Robotics and Machine Intelligence, Technical University of Munich, Germany. Corresponding Author's e-mail: <yu.li@tum.de>

<sup>2</sup> Mohamed Bin Zayed University of Artificial Intelligence, Abu Dhabi, UAE.

of the abdominal wall introduces non-ideal effects.

Thus, this paper aims at improving the control of RCM-constrained systems by providing:

- A reinterpretation of RCM as a rheonomic holonomic constraint embedded into a projection-based inverse-dynamics framework, reconciling task-level and kinematic formulations in a constraint-consistent [29] manner.
- A torque-level controller that unifies projection-based and dynamically consistent formulations, achieving accurate tool-tip tracking, smoother and more efficient torque behavior, and reliable RCM constraint satisfaction under insertion-depth variation and trocar motion.
- Extensive validation in simulation and on a RAMIS training platform, benchmarking against two relevant category of dynamical controllers with respect RCM adaption and constraint-consistency improvement. The proposed controller is further validated under clinically relevant conditions including spiral trajectories, variable insertion depth, moving trocars, and intentional human interaction.

The remainder of the paper is organized as follows: Section II reviews the background on projection-based constrained dynamics, Section III presents the proposed RCM constraint kinematics and controller design, Section IV reports simulation and experimental validation, and Section V discusses limitations and concludes the work.

## II. Preliminaries

We consider the joint-space dynamics of an  $n \in \mathbb{N}$  DoF manipulator subject to external interaction and  $k \in \mathbb{N}$  independent kinematic constraints, given by

$$\mathbf{M}\ddot{\mathbf{q}} + \mathbf{h} = \boldsymbol{\tau} + \mathbf{J}_c^T \mathbf{f}_c + \boldsymbol{\tau}_{ext}, \quad (1)$$

where  $\mathbf{q} \in \mathbb{R}^n$  is the joint configuration,  $\mathbf{M} \in \mathbb{R}^{n \times n}$  is the symmetric positive-definite inertia matrix,  $\mathbf{h} \in \mathbb{R}^n$  collects Coriolis, centrifugal, and gravitational torques,  $\boldsymbol{\tau} \in \mathbb{R}^n$  is the control input,  $\boldsymbol{\tau}_{ext} \in \mathbb{R}^n$  is the external torque, and  $\mathbf{f}_c \in \mathbb{R}^k$  is the generalized constraint force associated with the Jacobian  $\mathbf{J}_c \in \mathbb{R}^{k \times n}$ . The constraints satisfy  $\mathbf{J}_c \dot{\mathbf{q}} = \mathbf{0}$ , with  $\mathbf{J}_c$  assumed to have full row rank.

To separate constrained and free-motion dynamics, we introduce the orthogonal projector

$$\mathbf{P} = \mathbf{I} - \mathbf{J}_c^\dagger \mathbf{J}_c,$$

where  $(\cdot)^\dagger$  denotes the Moore–Penrose pseudoinverse. The operator  $\mathbf{P}$  projects onto the null space of  $\mathbf{J}_c$  and satisfies  $\mathbf{P}\dot{\mathbf{q}} = \dot{\mathbf{q}}$  for all  $\dot{\mathbf{q}} \in \mathcal{N}(\mathbf{J}_c)$  where  $\mathcal{N}(\cdot)$  defines the null-space. It is worthy noting that  $\mathbf{P}$  is idempotent, i.e.,  $\mathbf{P}^2 = \mathbf{P} = \mathbf{P}^T$ . Projecting (1) onto the free-motion subspace, it has

$$\mathbf{P}\mathbf{M}\ddot{\mathbf{q}} + \mathbf{P}\mathbf{h} = \mathbf{P}(\boldsymbol{\tau} + \boldsymbol{\tau}_{ext}). \quad (2)$$

Then, we decompose the control input torque into free-motion and constrained components,

$$\boldsymbol{\tau} = \boldsymbol{\tau}_\parallel \oplus \boldsymbol{\tau}_\perp, \quad (3)$$

where  $\boldsymbol{\tau}_\parallel := \mathbf{P}^\dagger \mathbf{P} \boldsymbol{\tau}_f$  lies in the free-motion subspace,  $\boldsymbol{\tau}_\perp := (\mathbf{I} - \mathbf{P}^\dagger \mathbf{P}) \boldsymbol{\tau}_c$  in the constrained subspace, and  $\boldsymbol{\tau}_f, \boldsymbol{\tau}_c$  denote free-space and constrained-space control inputs, respectively. The generalized inverse  $\mathbf{P}^\dagger$  is chosen dynamically consistent. Since  $\boldsymbol{\tau}_\perp$  does not contribute to motion, all free-space tasks such as trajectory tracking and null-space compliance are executed through  $\boldsymbol{\tau}_f$ .

For all admissible velocities  $\dot{\mathbf{q}} \in \mathcal{N}(\mathbf{J}_c)$ , it holds that  $(\mathbf{I} - \mathbf{P})\dot{\mathbf{q}} = \mathbf{0}$ . Differentiating with respect to time gives

$$(\mathbf{I} - \mathbf{P})\ddot{\mathbf{q}} = \dot{\mathbf{P}}\dot{\mathbf{q}}, \quad \dot{\mathbf{P}} = -\mathbf{J}_c^\dagger \mathbf{J}_c. \quad (4)$$

Combining (2) and (4), the constrained dynamics becomes

$$\mathbf{M}_f \ddot{\mathbf{q}} + \mathbf{P}\mathbf{h} - \dot{\mathbf{P}}\dot{\mathbf{q}} = \mathbf{P}(\boldsymbol{\tau} + \boldsymbol{\tau}_{ext}), \quad (5)$$

where  $\mathbf{M}_f = \mathbf{P}\mathbf{M} + (\mathbf{I} - \mathbf{P})$  is nonsingular by construction. Pre-multiplying (5) with  $\mathbf{J}\mathbf{M}_f^{-1}$  and substituting  $\mathbf{J}\ddot{\mathbf{q}} = \ddot{\mathbf{x}} - \dot{\mathbf{J}}\dot{\mathbf{q}}$ , the operational-space dynamics follows

$$\boldsymbol{\Lambda}_f \ddot{\mathbf{x}} + \underbrace{\boldsymbol{\Lambda}_f (\mathbf{J}\mathbf{M}_f^{-1} \mathbf{P}\mathbf{h} - (\dot{\mathbf{J}} + \mathbf{J}\mathbf{M}_f^{-1} \dot{\mathbf{P}})\dot{\mathbf{q}})}_{\mathbf{h}_f} = \mathbf{f}_f + \mathbf{f}_{ext}, \quad (6)$$

where  $\boldsymbol{\Lambda}_f = (\mathbf{J}\mathbf{M}_f^{-1} \mathbf{P}\mathbf{J}^T)^{-1}$  is the task-space inertia,  $\mathbf{h}_f$  is the bias force, and  $\mathbf{f}_{ext} = \mathbf{J}^{\#T} \boldsymbol{\tau}_{ext}$  is the projected external force with  $\mathbf{J}^{\#T} = (\mathbf{J}\mathbf{M}_f^{-1} \mathbf{P}\mathbf{J}^T)^{-1} \mathbf{J}\mathbf{M}_f^{-1} \mathbf{P}$ . To complete a free space task, the PD+ type controller is designed,

$$\mathbf{f}_f = \boldsymbol{\Lambda}_f \ddot{\mathbf{x}}_d + \mathbf{K}_{f,D} \dot{\mathbf{e}} + \mathbf{K}_{f,P} \mathbf{e} + \mathbf{h}_f, \quad (7)$$

where tracking error  $\mathbf{e} = \mathbf{x}_d - \mathbf{x}$  and positive-definite gains are  $\mathbf{K}_{f,P}, \mathbf{K}_{f,D}$ . The corresponding joint torque input is

$$\boldsymbol{\tau}_f = \mathbf{J}^T \mathbf{f}_f + \bar{\mathbf{N}} \boldsymbol{\tau}_0, \quad (8)$$

where  $\bar{\mathbf{N}} = \mathbf{I} - \mathbf{J}^T \mathbf{J}^{\#T}$  is the dynamically consistent null-space projector, and  $\boldsymbol{\tau}_0$  is an auxiliary null-space input for secondary objectives lying in the free motion space.

## III. Methods

Projection-based approaches have shown strong results in constrained dynamics and have been widely applied to constrained force regulation by designing the torque component  $\boldsymbol{\tau}_\perp$  in the constrained space [26], [27]. However, most existing works assume that kinematic constraints are inherently determined by the physical environment. The RCM constraint differs from this assumption, as it originates from the visco-elastic behavior of the abdomen [21] and may vary over time [7], making it a holonomic but rheonomic constraint rather than a scleromic one. Prior work has further interpreted the RCM constraint either as a kinematic or task-space constraint [29]. Hence, we propose a projected constraint-consistent controller

by mitigating the boundary between projection-based formulations [28] and operational-space control [23], accounting for the RCM constraint.

### A. RCM Kinematics from Projection

Let the reference pose of the surgical tool be  $(\mathbf{p}_r, \mathbf{R}_r) \in \mathbb{R}^3 \times \text{SO}(3)$ , where  $\mathbf{p}_r$  is the reference position and  $\mathbf{R}_r$  its orientation. Let the trocar point be  $\mathbf{p}_c(t)$ , which may move with known velocity  $\dot{\mathbf{p}}_c(t)$ . Two common formulations of RCM kinematics exist in the literature: the 3D formulation [14] and the 2D formulation [13]. To prepare for our later projection-based controller, we reinterpret both approaches by expressing them in the local tool-reference frame (the  $r$ -frame), as detailed in Fig. 2 with RCM kinematics. This ensures consistency with the projection formulation introduced in Section II, while maintaining equivalence to the original derivations.

The projected residual is defined as the orthogonal projection of the residual vector onto the  $r$ -frame. This approach adapts the idea presented in [14] by formulating the projection in the  $r$ -frame rather than the base frame.

$$\mathbf{x}_{p,rcm,3D} = \mathbf{R}_r^T \mathbf{p}_{cr} \in \mathbb{R}^3 \quad (9)$$

with  $\mathbf{p}_{cr} = \mathbf{p}_r - \mathbf{p}_c$ . The associated Jacobian with respect to  $\mathbf{p}_c$  is

$$\begin{bmatrix} \mathbf{J}_{p,c} \\ \mathbf{J}_{\omega,c} \end{bmatrix} = \begin{bmatrix} \mathbf{I}_{3 \times 3} & -\mathbf{p}_{cr}^\wedge \\ \mathbf{0}_{3 \times 3} & \mathbf{I}_{3 \times 3} \end{bmatrix} \begin{bmatrix} \mathbf{J}_{p,r} \\ \mathbf{J}_{\omega,r} \end{bmatrix}, \quad (10)$$

where  $\mathbf{J}_{p,r}$  and  $\mathbf{J}_{\omega,r}$  are the translational and angular parts of the Jacobian at the tool reference, while  $\mathbf{J}_{p,c}$  and  $\mathbf{J}_{\omega,c}$  correspond to the trocar point. The RCM Jacobian then follows the orthogonal projection correspondingly, i.e.,

$$\mathbf{J}_{rcm,3D} = \mathbf{R}_r^T \mathbf{J}_{c,p}. \quad (11)$$

Consequently, the projected velocity residual becomes

$$\dot{\mathbf{x}}_{p,rcm,3D} = \mathbf{J}_{rcm,3D} \dot{\mathbf{q}} - \mathbf{R}_r^T \dot{\mathbf{p}}_c. \quad (12)$$

Notably, for the 2D case following [13], we define a planar basis  $\mathbf{B}_r \in \mathbb{R}^{3 \times 2}$  by taking the first two columns of  $\mathbf{R}_r$ . Replacing  $\mathbf{R}_r$  with  $\mathbf{B}_r$  in (9)–(12), we obtain the corresponding Jacobian  $\mathbf{J}_{rcm,2D}$ , and 2D residual  $\mathbf{x}_{p,rcm,2D}$  and velocity  $\dot{\mathbf{x}}_{p,rcm,2D}$ .

### B. Constraint-consistent control

Non-ideal kinematic or task-level constraints can be described by general rheonomic holonomic conditions, i.e.,

$$\Phi_c(\mathbf{q}, t) = \mathbf{x}_c(t) \in \mathbb{R}^k, \quad (13)$$

where  $\mathbf{x}_c(t)$  denotes the time variant residual constraint coordinate.  $(\cdot)_c$  represents not only the placeholder of different RCM constraint formulations but also for any generic constraints. To obtain the velocity and

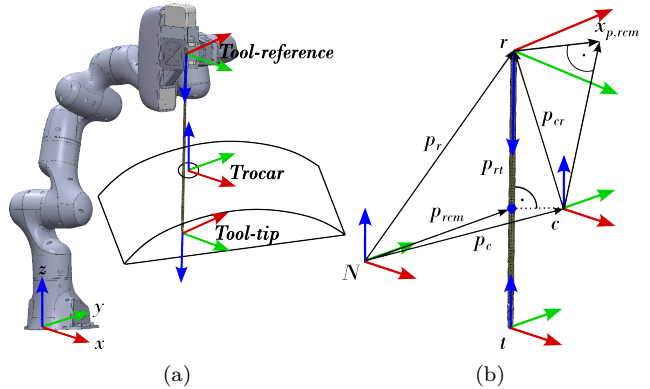


Fig. 2: (a) Illustration of the considered scenario, where the shaft of a surgical tool attached to a SRM (see [22] for details) is passing through the RCM (located at the trocar point). The relevant frames associated with the trocar and the tip and reference of the tool are depicted. (b) Model associated to the RCM projection residual expressed from the tool-reference  $r$ -frame.  $c$  and  $t$  are the frames related to the trocar and the tip of the tool, respectively.

acceleration relationships, we differentiate the constraint equation (13) with respect to time as follows

$$\frac{\partial \Phi_c}{\partial \mathbf{q}} \dot{\mathbf{q}} + \frac{\partial \Phi_c}{\partial t} = \dot{\mathbf{x}}_c, \quad \frac{\partial^2 \Phi_c}{\partial \mathbf{q}^2} \dot{\mathbf{q}} + \frac{\partial \Phi_c}{\partial \mathbf{q}} \ddot{\mathbf{q}} + \frac{\partial^2 \Phi_c}{\partial t^2} = \ddot{\mathbf{x}}_c. \quad (14)$$

For brevity, we define the Jacobian of  $\mathbf{x}_c$  as  $\mathbf{J}_c = \partial \Phi_c / \partial \mathbf{q}$  and the lumped nonlinear bias term at acceleration level  $\mathbf{b}_c := \frac{\partial^2 \Phi_c}{\partial \mathbf{q}^2} \dot{\mathbf{q}} + \frac{\partial^2 \Phi_c}{\partial t^2}$ <sup>1</sup>. We then obtain the acceleration-level equivalence subject to constraint

$$\mathbf{J}_c \ddot{\mathbf{q}} = \ddot{\mathbf{x}}_c - \mathbf{b}_c. \quad (15)$$

Pre-multiplying by  $\mathbf{J}_c^\dagger$  gives

$$(\mathbf{I} - \mathbf{P}) \ddot{\mathbf{q}} = \mathbf{J}_c^\dagger (\ddot{\mathbf{x}}_c - \mathbf{b}_c). \quad (16)$$

Thus, the joint acceleration decomposes as

$$\ddot{\mathbf{q}} = \ddot{\mathbf{q}}_{\parallel} \oplus \ddot{\mathbf{q}}_{\perp},$$

with  $\ddot{\mathbf{q}}_{\parallel} = \mathbf{P} \ddot{\mathbf{q}}$  and  $\ddot{\mathbf{q}}_{\perp} = (\mathbf{I} - \mathbf{P}) \ddot{\mathbf{q}}$ . Substituting the dynamics (1), we obtain

$$\ddot{\mathbf{q}} = \mathbf{J}_{rcm}^\dagger (\ddot{\mathbf{x}}_c - \mathbf{b}_c) + \mathbf{P} \mathbf{M}^{-1} (\boldsymbol{\tau} + \boldsymbol{\tau}_{ext} - \mathbf{h}),$$

which combines constrained and unconstrained dynamics in the sense of Gauss's principle [19]. Accordingly, (5) updates to

$$\mathbf{M}_f \ddot{\mathbf{q}} = \mathbf{P} (\boldsymbol{\tau}_f + \boldsymbol{\tau}_{ext} - \mathbf{h}) - \mathbf{J}_{rcm}^\dagger (\ddot{\mathbf{x}}_c - \mathbf{b}_c). \quad (17)$$

The corresponding operational formulation (6) is obtained by substituting

$$\mathbf{h}_f = \boldsymbol{\Lambda}_f (\mathbf{J} \mathbf{M}_f^{-1} \mathbf{P} \mathbf{h} - \dot{\mathbf{J}} \dot{\mathbf{q}} + \mathbf{J} \mathbf{M}_f^{-1} \mathbf{J}_{rcm}^\dagger (\ddot{\mathbf{x}}_c - \mathbf{b}_c)). \quad (18)$$

Hence, the operational-space control law (7) applies with the updated  $\mathbf{h}_f$ .

<sup>1</sup>For brevity, the computation is not analytically elaborated with respect to different RCM or any constraint implementations.

To stabilize the residual dynamics, the constraint acceleration is designed as

$$\ddot{\mathbf{x}}_c = \ddot{\mathbf{x}}_{c,d} - \mathbf{\Lambda}_c^{-1}(\mathbf{K}_{c,D}\dot{\mathbf{x}}_c + \mathbf{K}_{c,P}\tilde{\mathbf{x}}_c) + \mathbf{b}_c, \quad (19)$$

where  $\tilde{\mathbf{x}}_c = \mathbf{x}_c - \mathbf{x}_{c,d}$  denotes the constraint error,  $\mathbf{K}_{c,P}, \mathbf{K}_{c,D} \succ 0$  are gain matrices, and  $\mathbf{\Lambda}_c = (\mathbf{J}_c \mathbf{M}^{-1} \mathbf{J}_c^T)^{-1}$  is the constraint-space inertia. For most of the cases (e.g. RCM constraints),  $\mathbf{x}_{c,d} = \mathbf{0}$  will be defined for perfect satisfactions.

The associated constrained torque in (3) is then designed as

$$\boldsymbol{\tau}_c = \mathbf{J}_c^T(\mathbf{\Lambda}_c \ddot{\mathbf{x}}_c + \mathbf{J}_c \mathbf{M}^{-1} \mathbf{h}). \quad (20)$$

In analogy to the free-space formulation, this ensures that  $\mathbf{x}_{p,rcm}$  and its derivatives converge to zero. Any disturbance induced by the additional constraint dynamics is compensated by updating  $\dot{\mathbf{x}}_c$  via (19).

Remark 1. To enhance robustness, we extend the control law with a disturbance estimate  $\hat{\boldsymbol{\tau}}_{ext}$ , such that

$$\hat{\boldsymbol{\tau}} = \boldsymbol{\tau}_{\parallel} \oplus \boldsymbol{\tau}_{\perp} + \hat{\boldsymbol{\tau}}_{ext}. \quad (21)$$

The estimate  $\hat{\boldsymbol{\tau}}_{ext}$  can be decomposed into free and constrained components using  $\mathbf{P}$  and is obtained via a momentum-based observer with sign inversion, so that  $\hat{\boldsymbol{\tau}}_{ext} + \boldsymbol{\tau}_{ext} \rightarrow 0$  [30]. Finally, null-space compliance is introduced through

$$\boldsymbol{\tau}_0 = -\mathbf{K}_{n,D}\dot{\tilde{\mathbf{q}}} - \mathbf{K}_{n,P}\tilde{\mathbf{q}}, \quad (22)$$

where  $\tilde{\mathbf{q}} = \mathbf{q} - \mathbf{q}_{init}$  is defined relative to the initial configuration, and  $\mathbf{K}_{n,P}, \mathbf{K}_{n,D} \succ 0$  are null-space impedance gains. The final control input  $\hat{\boldsymbol{\tau}}$  thus replaces  $\boldsymbol{\tau}$  in (1) under disturbances.

### C. Baseline of projection controllers for comparison

1) Projection Jacobian approach: For comparison, we first outline an alternative operational-space formulation that forms the core of the state-of-the-art admittance controller [13]. The dynamics in operational space are expressed as

$$\mathbf{\Lambda}_E \ddot{\mathbf{x}} + \mathbf{H}_E = \begin{bmatrix} \mathbf{f}_c \\ \mathbf{f}_n \end{bmatrix}, \quad (23)$$

where

$$\mathbf{\Lambda}_E = \mathbf{J}_E^{-T} \mathbf{M} \mathbf{J}_E^{-1} = \begin{bmatrix} \mathbf{\Lambda}_c & 0 \\ 0 & \mathbf{\Lambda}_n \end{bmatrix}, \quad (24)$$

$$\mathbf{\Lambda}_c = (\mathbf{J}_c \mathbf{M}^{-1} \mathbf{J}_c^T)^{-1}, \quad (25)$$

$$\mathbf{\Lambda}_n = \mathbf{Z}^T \mathbf{M} \mathbf{Z}, \quad (26)$$

$$\mathbf{H}_E = \mathbf{\Lambda}_E \left( \begin{bmatrix} \mathbf{J}_c \\ \mathbf{Z}^{\#} \end{bmatrix} \mathbf{M}^{-1} \mathbf{h} - \begin{bmatrix} \dot{\mathbf{J}}_c \\ \frac{d}{dt} \mathbf{Z}^{\#} \end{bmatrix} \dot{\mathbf{q}} \right). \quad (27)$$

The extended Jacobian  $\mathbf{J}_E$  is defined by

$$\begin{bmatrix} \dot{\mathbf{x}}_c \\ \dot{\mathbf{x}}_n \end{bmatrix} = \underbrace{\begin{bmatrix} \mathbf{J}_c \\ \mathbf{Z}^{\#} \end{bmatrix}}_{\mathbf{J}_E} \dot{\mathbf{q}}, \quad (28)$$

where  $\dot{\mathbf{x}}_n$  denotes the null-space velocity orthogonal to the constraint space, and  $\mathbf{Z}^{\#} = (\mathbf{Z}^T \mathbf{M} \mathbf{Z})^{-1} \mathbf{Z}^T \mathbf{M}$ . The corresponding torque input is

$$\boldsymbol{\tau} = \mathbf{J}_E^T \begin{bmatrix} \mathbf{f}_c \\ \mathbf{Z}^T \mathbf{J}_E^T \mathbf{f}_f \end{bmatrix} + \mathbf{H}_E + \hat{\boldsymbol{\tau}}_{ext}, \quad (29)$$

where the constraint  $\mathbf{J} \mathbf{Z} = \mathbf{0}$  holds and  $\mathbf{Z}$  is chosen following [31]. For simplicity and comparability, we restrict to the static RCM case with  $\dot{\mathbf{p}}_c = \mathbf{0}$ . The constrained force  $\mathbf{f}_c$  is implemented through a PD law relative to  $-\mathbf{x}_c$ ,

$$\mathbf{f}_c = \mathbf{\Lambda}_c \ddot{\mathbf{x}}_{c,d} - \mathbf{K}_{c,D} \dot{\mathbf{x}}_c - \mathbf{K}_{c,P} \tilde{\mathbf{x}}_c, \quad (30)$$

While the free-space force  $\mathbf{f}_f$  follows the PD control likewise of (7).

2) Dynamical Udwadia–Kalaba controller: We also reformulate an existing torque controller [20], originally derived from a dynamically consistent framework, but lacking explicit constraint consistency in the residual dynamics. Starting from the constraint relation (15), the inverse dynamics are decomposed according to the Udwadia–Kalaba (U–K) principle [19]:

$$\mathbf{M} \ddot{\mathbf{q}} = \mathbf{Q} + \mathbf{Q}_{ic} + \mathbf{Q}_{nic} + \mathbf{h} + \hat{\boldsymbol{\tau}}_{ext}, \quad (31)$$

where  $\mathbf{Q}$ ,  $\mathbf{Q}_{ic}$ , and  $\mathbf{Q}_{nic}$  denote the contributions from free motion, ideal constraints, and non-ideal constraints, respectively:

$$\mathbf{Q} = \boldsymbol{\tau}^{\#} - \mathbf{h}, \quad (32)$$

$$\mathbf{Q}_{ic} = \mathbf{M}^{1/2} \mathbf{\Pi}^{\dagger} (\mathbf{b}_{ic} - \mathbf{J}_c \mathbf{M}^{-1} \mathbf{Q}), \quad (33)$$

$$\mathbf{Q}_{nic} = \mathbf{M}^{1/2} \left[ \mathbf{I} - \mathbf{\Pi}^{\dagger} \mathbf{J}_c \mathbf{M}^{-1/2} \right] \mathbf{M}^{-1/2} \boldsymbol{\tau}_{nic}, \quad (34)$$

with  $\boldsymbol{\tau}^{\#}$  the free-space torque (designed as Cartesian PD+ with optional null-space term),  $\mathbf{\Pi} = \mathbf{J}_c \mathbf{M}^{-1/2}$ , and

$$\boldsymbol{\tau}_{nic} = \mathbf{J}_c^T (\mathbf{\Lambda}_c \ddot{\mathbf{x}}_{c,d} - \mathbf{K}_{c,D} \dot{\mathbf{x}}_c - \mathbf{K}_{c,P} \tilde{\mathbf{x}}_c), \quad (35)$$

as in (20). Likely to the proposed controller, the term  $\mathbf{b}_{ic} = \mathbf{\Lambda}_c \ddot{\mathbf{x}}_{c,d} - \mathbf{K}_{c,D} \dot{\mathbf{x}}_c - \mathbf{K}_{c,P} \tilde{\mathbf{x}}_c$ , accounts for ideal rheonomic holonomic constraints and compensates for the part from non-ideal constraints minimization efforts  $\boldsymbol{\tau}_{nic}$ . Unlike [20], where  $\boldsymbol{\tau}_{nic}$  is simply added to  $\mathbf{Q}$  and  $\mathbf{Q}_{ic}$ , here the non-ideal constraint is consistently projected into torque space, leading to a self-contained constraint-consistent formulation.

## IV. Results

In this section, the proposed controller is first validated through simulation and experiments in comparison with baseline controllers. Subsequently, we examine its performance in dynamic and human-interactive tasks to demonstrate reliability in practice.

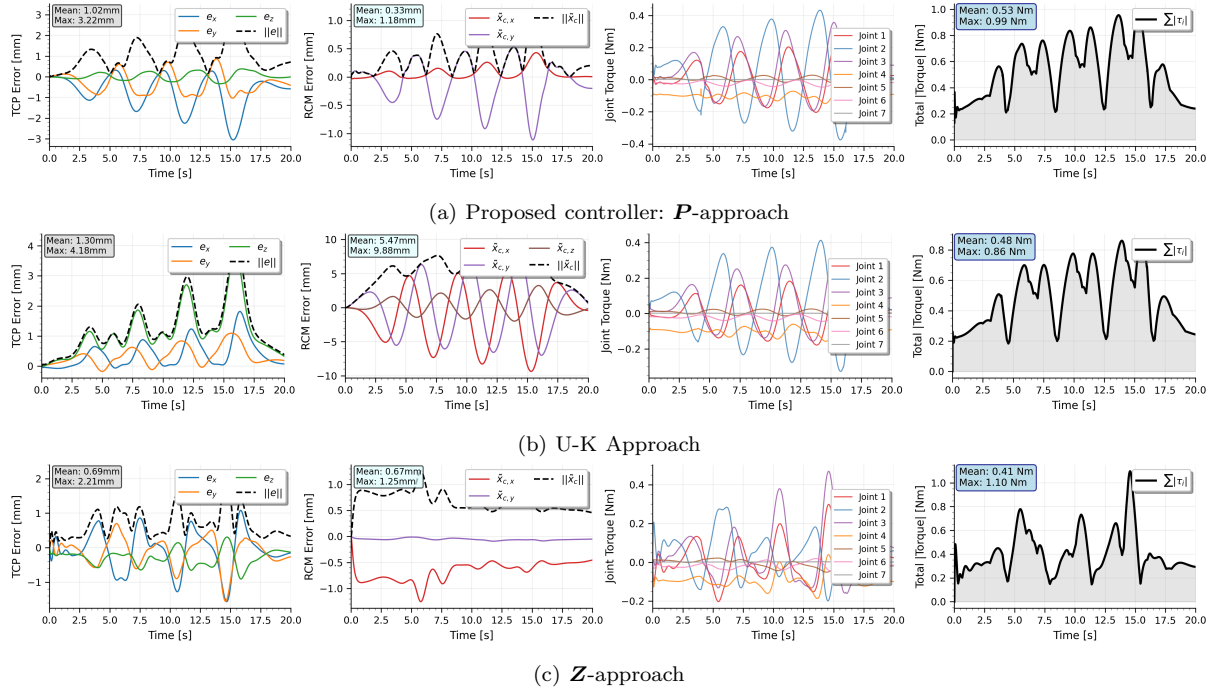


Fig. 3: Simulation results: controllers performance compared through TCP tracking, RCM constraint satisfactions and in joint torques.

### A. Task implementation

For benchmarking, the controllers are implemented following their original formulations. The U-K approach of Minelli et al. [20] is evaluated under 3D RCM constraints, while the other two approaches adopt the 2D formulation. Accordingly, goals are set  $\mathbf{x}_{c,d}$  and its derivatives to zero and all terms  $(\cdot)_c$  are instantiated as  $(\cdot)_{p,rcm,3D}$  or  $(\cdot)_{p,rcm,2D}$ , respectively,

A dynamically challenging spiral trajectory  $\mathbf{p}_{t,d}(t)$  is generated along the robot's  $z$ -axis. The trajectory has a radius of  $r = 0.02$  m, a pitch of 0.015 m, and a trapezoidal velocity profile over a duration of  $T = 20$  s. The free space command is set to  $\mathbf{x}_d = \mathbf{p}_{t,d}$  and  $\mathbf{x} = \mathbf{p}_t$  as well with respect to their derivatives.

The trocar position  $\mathbf{p}_c$  is initialized from the starting configuration  $(\mathbf{p}_r(0), \mathbf{p}_t(0))$  using a scaling factor  $\alpha$ :

$$\mathbf{p}_c = \mathbf{p}_r(0) + \alpha (\mathbf{p}_t(0) - \mathbf{p}_r(0)).$$

The physical insertion depth is  $\alpha \cdot L_{\text{tool}}$ , where the tool length is  $L_{\text{tool}} = 0.59$  m. A larger  $\alpha$  corresponds to a shallower insertion.

In practice, trocar motion can be induced by patient breathing or heartbeat [7], typically with excursions of about 3–8 cm<sup>2</sup>. To emulate this effect, a 0.2 Hz sinusoidal motion of  $\mathbf{p}_c$  along the  $z$ -axis with amplitude  $\pm 4$  cm is predefined in the experiments.

<sup>2</sup><https://web.archive.org/web/20100212114324/http://mtsu32.mtsu.edu:11259/percussdiaphexcursion.htm>

### B. Performance validation through simulation

To validate the effectiveness of the proposed constraint-consistent controller (denoted  $\mathbf{P}$ -approach), we compare it with two state-of-the-art controllers: the projection Jacobian controller ( $\mathbf{Z}$ -approach, Sec. III-C.1) and the dynamical U-K controller (Sec. III-C.2).

A MuJoCo simulation environment is built with a timestep of 1 ms. Soft objects from the MuJoCo assets are imported to mimic soft kinematic constraints, allowing partial penetration by tuning impedance factors. For simplicity, moving trocar conditions are omitted in simulation. Controller gains are tuned as follows: a)  $\mathbf{P}$ - and  $\mathbf{Z}$ -approaches are tuned for comparable tip tracking and RCM constraint satisfaction, as shown in the error plots of Fig. 3; b) the same gains from (a) are directly applied to the U-K approach for consistency; c) derivative gains are set element-wise as  $k_{D,i} = 2\sqrt{k_{P,i}}$  for all controllers.

Compared to the  $\mathbf{Z}$ -approach, which shows mean absolute torque of 0.41 Nm and peak torque of 1.10 Nm, the proposed  $\mathbf{P}$ -approach consumes slightly more torque (mean 0.53 Nm, peak 0.99 Nm). However, the  $\mathbf{P}$ -approach produces smoother and more consistent torque trajectories, both at the joint level and in the total torque profile, since  $\mathbf{Z}$ -approach shows an aperiodic and jerk profile within the periodic trajectory following task, highlighting with a 11% higher of peak torque. Compared to the U-K approach, both methods yield smooth torque evolution, but the proposed controller achieves significantly higher accuracy in tip tracking and RCM constraint satisfaction. It is also worth noting that the U-K approach, when implemented solely with the

additional  $\tau_{nic}$  term as in [20], exhibits instability in simulation within the selected gain range.

### C. Performance validation through experiment

1) Comparative evaluation of the proposed controller: Experiments are conducted on a Franka Research 3 (FR3) robot arm with a real-time loop running at 1 kHz under Ubuntu 22.04 with a real-time kernel.

To further validate the simulation results, we compare the proposed controller ( $\mathbf{P}$ -approach) with the  $\mathbf{Z}$ -approach. The U-K approach could not be stably implemented with the same (or similar) gains as the  $\mathbf{P}$ -approach, likely due to numerical issues arising from heavy matrix manipulations and sensitivity to modeling errors. The gains of the  $\mathbf{Z}$ -approach are tuned in the same manner as in simulation<sup>3</sup>, and the tracking error trajectories and statistics are shown in Fig. 4.

The proposed controller achieves better RCM constraint satisfaction while showing slightly weaker tip tracking than the  $\mathbf{Z}$ -approach. Nevertheless, the total torque consumption of the  $\mathbf{P}$ -approach, computed as the sum of absolute joint torques, is about half of that of the  $\mathbf{Z}$ -approach. Moreover, the peak torques of the  $\mathbf{Z}$ -approach are 77% higher than those of the proposed controller. This reduction is explained by the orthogonal decomposition, which minimizes overall torques as  $\|\boldsymbol{\tau}\| \leq \|\mathbf{P}^\dagger \mathbf{P} \boldsymbol{\tau}\| + \|(\mathbf{I} - \mathbf{P}^\dagger \mathbf{P}) \boldsymbol{\tau}\|$  in the constraint-consistent formulation. Additionally, the  $\mathbf{Z}$ -approach produces more aggressive torque trajectories, consistent with the non-smooth behavior observed in simulation due to the lack of a dynamical constraint-consistent formulation, which likely amplifies overall torque consumption. It is notable, that the  $\mathbf{Z}$ -approach naturally faces non-passive issue [32], while the proposed controller through the projection-based formulation unified by operational space control [23] stays inherently passive.

2) Dynamical task feasibility experiment: The insertion depth varies with the surgical objective and can be adjusted either by semi-autonomous guidance of the torque-controlled manipulator or by teleoperation. To investigate this, experiments are conducted at three insertion depths, corresponding to scaling factors  $\alpha = 75\%, 50\%, 25\%$ . The results are visualized in Fig. 5(a–c).

For spatial visualization, the RCM position is computed following [14] as

$$\mathbf{p}_{rcm} = \mathbf{p}_r + \frac{1}{L_{tool}^2} \mathbf{p}_{rt}^T \mathbf{p}_{rc} \mathbf{p}_{rt},$$

where  $\mathbf{p}_{rt} = \mathbf{p}_t - \mathbf{p}_r$  with the tool-tip position  $\mathbf{p}_t$  expressed in the base frame (Fig. 2b).

The results displayed in Fig. 5(a–c) shows a good spatial correspondence between the desired  $\mathbf{p}_c$  (blue cross) and the obtained  $\mathbf{p}_{rcm}$  values (magenta circles) as well on projected residual plot. However, shallower insertions

<sup>3</sup>For transparency, the proportional gains applied to the tool tip and RCM tasks are 1000 and 1500 N/m, respectively, in diagonal form.

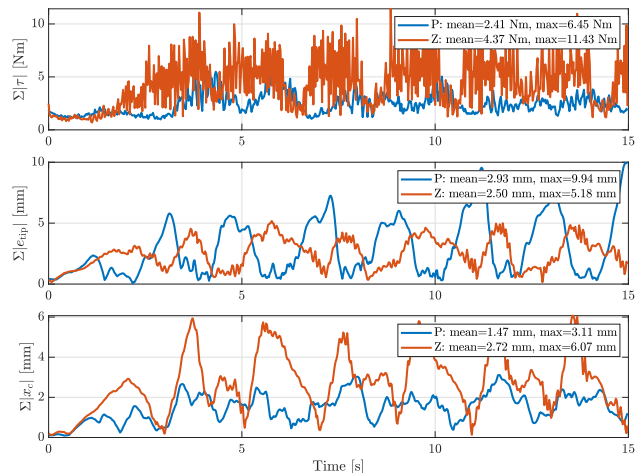


Fig. 4: Comparison of torque consumption between proposed (blue) and Z-approach (orange). The tracking and RCM constraint residual results have been compared to show the fairness of gain selection.

TABLE I: Mean Absolute Error ( $\times 10^{-3}$  meter)

Case	Tip Error (X, Y, Z)			RCM Residual (X, Y)	
a	0.5066	0.2504	0.8444	0.4152	0.6824
b	0.9992	0.9972	0.9155	0.7336	0.7079
c	3.0231	3.0567	0.9449	2.7085	1.6267
d	0.9440	0.9854	0.9369	0.7995	0.7276

(smaller  $\alpha$ ) make both tip tracking and RCM constraint satisfaction more difficult. The tool-reference motion  $\mathbf{p}_r$  (green trace) increases by roughly a factor of three from case (a) to case (c). This lever-arm effect means that shallower insertion amplifies lateral displacements for the same angular deviation. Consequently, the system undergoes faster motions, which magnify errors caused by model mismatches, in particular due to discrepancies in the customized surgical tool drive unit. Consistently, the tip error also scales with the lever arm, being about three times larger in case (c) than in case (a). The quantitative results are summarized in Table I.

Finally, rheonomic effects are evaluated by activating trocar motion as described in Sec. IV-A. The numerical error in Fig. 5(d) and the mean absolute error in Table I remain small and close to those of case (c) under the same insertion depth. This confirms that the rheonomic constraints are successfully handled by the proposed controller.

### D. Human Interaction

As shown by Sadeghian et al. [33], [34], compensating external torques enhances disturbance rejection in both primary and secondary tasks. We conducted experiments in which the manipulator followed the same spiral trajectory of 20 s duration at 50% insertion depth. Incorporating the observed external torques increased robustness, as demonstrated in Fig. 6(b), compared to Fig. 6(a) without  $\hat{\boldsymbol{\tau}}_{ext}$ . When an external torque was

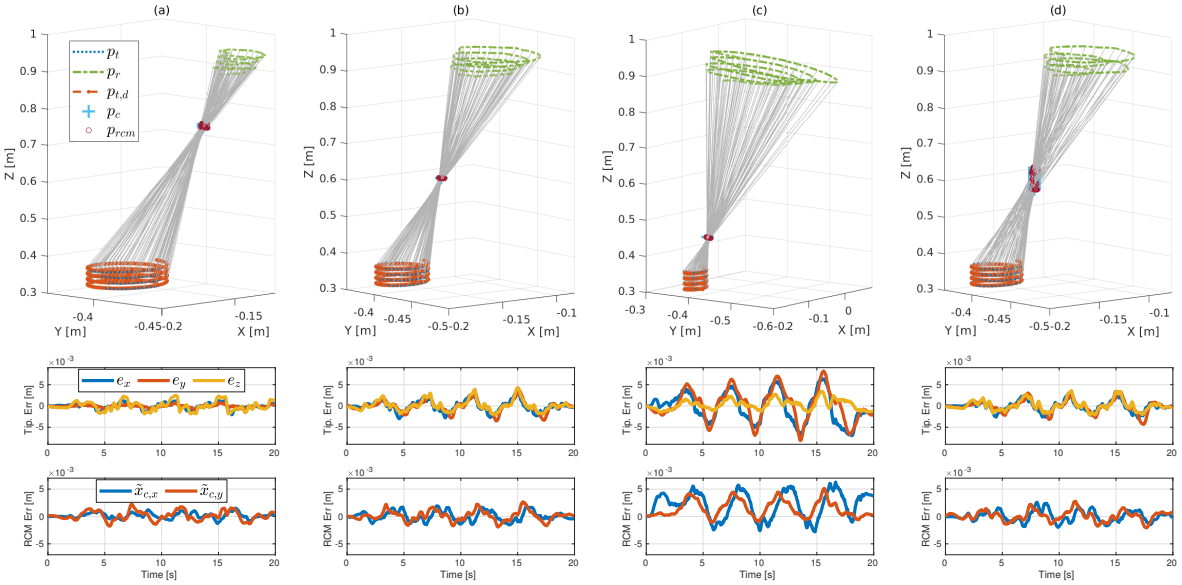


Fig. 5: Experiment results of proposed controller on dynamical cases: (a-c) show the group with respect to insertion depth from 75% to 25 % of the total tool length, respectively. (d) shows the result with respect moving trocar. From top to bottom are showing 3D tracking visualization, tool tip tracking and RCM projection residual results, respectively.

exerted at the flange, both tracking and RCM errors increased slightly but remained within acceptable limits.

Intentional interaction was not suppressed but expressed through null-space compliance according to (22). In the experiment, push–pull forces were applied to the second link of the robot, mimicking arm bending into different attack angles (see Fig. 2b). The observed torque at joint 2 and the corresponding induced torque at joint 1 are shown in Fig. 6(c). A joint stiffness of 5 Nm/rad with sufficient damping was applied. Several joints, notably  $q_1$ ,  $q_3$ ,  $q_5$ , and  $q_6$ , actively contributed to the compliant null-space response at different phases of motion. In theory, null-space compliance should not degrade tip tracking or RCM satisfaction; in practice, however, a small increase in errors is observed in Fig. 6(c) compared to the baseline in Fig. 6(a).

## V. Discussion and conclusion

**Discussion.** This work addresses rheonomic holonomic constraints by formulating task and kinematic conditions within a projected constraint-consistent controller. The approach was validated in clinically relevant dynamic control scenarios for RCM in minimally invasive robotic surgery, demonstrating smoother and more efficient torque behavior, improved RCM constraint satisfaction, and greater robustness compared to state-of-the-art baselines. These advantages arise from unifying projection-based and dynamically consistent formulations. Beyond these benefits, several limitations deserve discussion.

First, projection-based formulations remain numerically sensitive [29]. Even small modeling errors or ill-conditioned Jacobians can destabilize the projector. Second, RCM kinematics are inherently depth-sensitive: due

to the lever-arm effect, control gains tuned for one insertion length may degrade performance at another, making it difficult to define a unified gain set. Third, although a PD(+) law was used for fair comparison, passivity-preserving extensions of the proposed controller exist and could enhance robustness, but were not explored here. Fourth, while torque smoothness has improved, residual high-frequency oscillations may degrade accuracy with long or flexible instruments in practical deployment, and the lack of direct tip sensing means forward kinematics remain the only feedback source. Fifth, null-space compliance, though enabling interaction, is configuration-dependent: in some poses, surgeons may not intuitively adjust the attack angle, suggesting that admittance control is still relevant. Finally, gain tuning itself poses a practical challenge: despite theoretical orthogonality, RCM and tip-task gains remain coupled, and adjusting one often affects the other. This interdependence was particularly evident in the  $Z$ - and U-K baselines and complicates fair cross-method comparison.

**Conclusion.** The proposed controller establishes a constraint-consistent torque paradigm for RCM-constrained surgical robotics and demonstrates clear advantages in improved joint torque smoothness, efficiency, and robustness. Future research should focus on reducing numerical sensitivity, mitigating depth dependence, integrating passivity-preserving designs, and exploring shared-control schemes that accommodate inequivalent task constraints.

## References

- [1] J. A. Smith Jr and S. D. Herrell, “Robotic-assisted laparoscopic prostatectomy: do minimally invasive approaches offer significant advantages?” *Journal of clinical oncology*, vol. 23, no. 32, pp. 8170–8175, 2005.

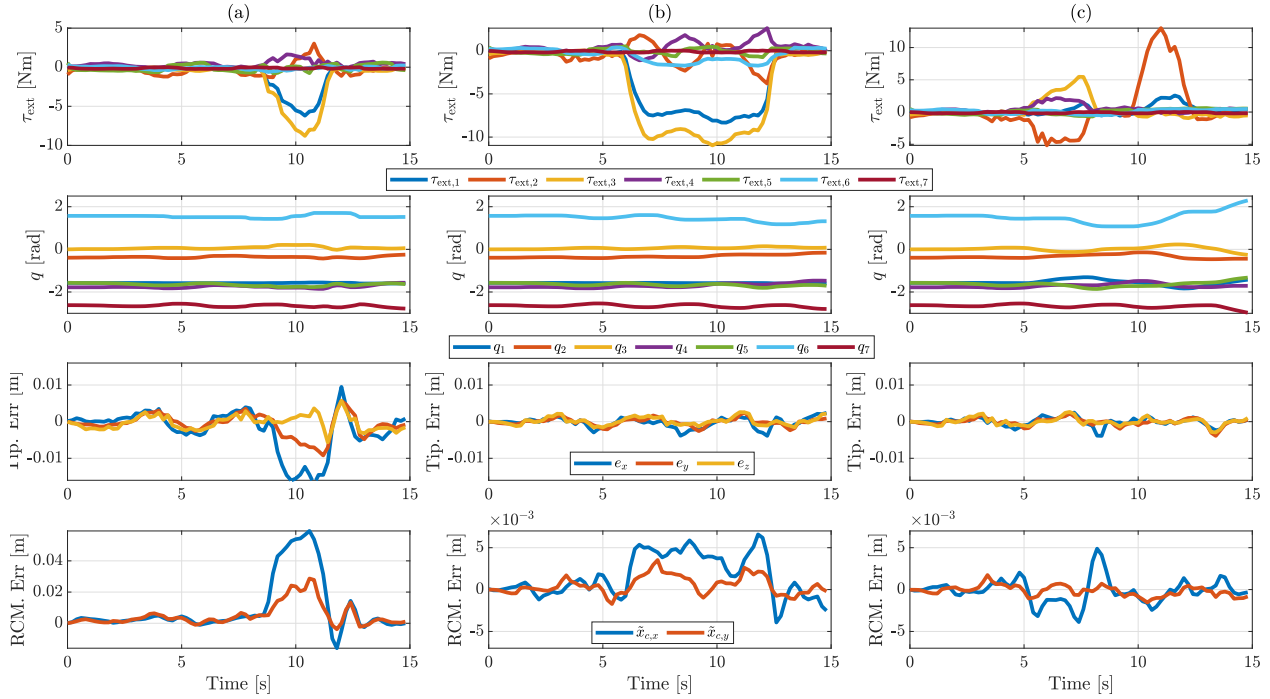


Fig. 6: Experiment results with respect to interaction scenarios: (respectively joint torques and position, tip tracking, and RCM projection residual errors) obtained during the controller evaluation involving human interactions. (a) shows no rejection on disturbance from the interaction at the flange that has been applied. (b) shows Interactions at the flange are rejected. While the intentional interaction induces desired null-space compliance in (c).

[2] E. Nugent, “The evaluation of fundamental ability in acquiring minimally invasive surgical skill sets,” Ph.D. dissertation, Royal College of Surgeons in Ireland, 2012.

[3] R. N. Elek and T. Haidegger, “Robot-assisted minimally invasive surgical skill assessment—manual and automated platforms,” *Acta Polytechnica Hungarica*, vol. 16, no. 8, pp. 141–169, 2019.

[4] J. Funda, R. H. Taylor, B. Eldridge, S. Gomory, and K. G. Gruben, “Constrained cartesian motion control for teleoperated surgical robots,” *IEEE Transactions on Robotics and Automation*, vol. 12, no. 3, pp. 453–465, 1996.

[5] S. Aksungur, “Remote center of motion (rcm) mechanisms for surgical operations,” *International Journal of Applied Mathematics Electronics and Computers*, vol. 3, no. 2, pp. 119–126, 2015.

[6] Z. Wang, W. Zhang, and X. Ding, “A family of rcm mechanisms: type synthesis and kinematics analysis,” *International Journal of Mechanical Sciences*, vol. 231, p. 107590, 2022.

[7] H. Sadeghian, F. Zokaei, and S. Hadian Jazi, “Constrained kinematic control in minimally invasive robotic surgery subject to remote center of motion constraint,” *Journal of intelligent & robotic systems*, vol. 95, pp. 901–913, 2019.

[8] N. Aghakhani, M. Geravand, N. Shahriari, M. Vendittelli, and G. Oriolo, “Task control with remote center of motion constraint for minimally invasive robotic surgery,” in 2013 IEEE international conference on robotics and automation. IEEE, 2013, pp. 5807–5812.

[9] A. Davila, J. Colan, and Y. Hasegawa, “Real-time inverse kinematics for robotic manipulation under remote center-of-motion constraint using memetic evolution,” *Journal of Computational Design and Engineering*, vol. 11, no. 3, pp. 248–264, 2024.

[10] W. Li, P. W. Y. Chiu, and Z. Li, “An accelerated finite-time convergent neural network for visual servoing of a flexible surgical endoscope with physical and rcm constraints,” *IEEE transactions on neural networks and learning systems*, vol. 31, no. 12, pp. 5272–5284, 2020.

[11] M. Liu, K. Liu, P. Zhu, G. Zhang, X. Ma, and M. Shang, “Data-Driven Remote Center of Cyclic Motion (RC<sup>2</sup>M) Control for Redundant Robots With Rod-Shaped End-Effectors,” *IEEE Transactions on Industrial Informatics*, vol. 20, no. 4, pp. 6772–6780, 2024.

[12] M. Minelli and C. Secchi, “Dynamic-based rcm torque controller for robotic-assisted minimally invasive surgery,” in 2021 IEEE/RSJ International Conference on Intelligent Robots and Systems (IROS). IEEE, 2021, pp. 733–740.

[13] T. Kastritsi and Z. Doulgeri, “A control method for time-variant rcm constraint in hands-on ramis procedures,” in 2021 29th Mediterranean Conference on Control and Automation (MED). IEEE, 2021, pp. 729–734.

[14] J. Sandoval, G. Poisson, and P. Vieyres, “A new kinematic formulation of the rcm constraint for redundant torque-controlled robots,” in 2017 IEEE/RSJ International Conference on Intelligent Robots and Systems (IROS). IEEE, 2017, pp. 4576–4581.

[15] H. Su, C. Yang, G. Ferrigno, and E. De Momi, “Improved human-robot collaborative control of redundant robot for teleoperated minimally invasive surgery,” *IEEE Robotics and Automation Letters*, vol. 4, no. 2, pp. 1447–1453, 2019.

[16] H. Su, W. Qi, J. Chen, and D. Zhang, “Fuzzy approximation-based task-space control of robot manipulators with remote center of motion constraint,” *IEEE Transactions on Fuzzy Systems*, vol. 30, no. 6, pp. 1564–1573, 2022.

[17] N. Piccinelli, G. Colombo-Taccani, and R. Muradore, “A passive convex optimal control algorithm for teleoperating a redundant robotic arm in minimally invasive surgery,” *International Journal of Robust and Nonlinear Control*, 2024.

[18] T. Kastritsi, T. P. Semetzidis, and Z. Doulgeri, “Passive bilateral surgical teleoperation with rcm and spatial constraints in the presence of time delays,” *IEEE Transactions on Robotics*, 2024.

[19] F. E. Udwadia and R. E. Kalaba, “On the foundations of analytical dynamics,” *International Journal of non-linear mechanics*, vol. 37, no. 6, pp. 1079–1090, 2002.

[20] M. Minelli and C. Secchi, “A torque controlled approach for virtual remote centre of motion implementation,” in 2022

IEEE/RSJ International Conference on Intelligent Robots and Systems (IROS). IEEE, 2022, pp. 4949–4956.

[21] M. Kirilova, S. Stoytchev, D. Pashkouleva, V. Tsenova, and R. Hristoskova, “Visco-elastic mechanical properties of human abdominal fascia,” *Journal of bodywork and movement therapies*, vol. 13, no. 4, p. 336, 2009.

[22] C. U. Kenanoglu, V. Le Mesle, G. Luarasi, H. Sadeghian, and S. Haddadin, “Design and evaluation of a surgical tool drive unit for sustainable training in robot-assisted minimally invasive surgery,” in 2024 10th IEEE RAS/EMBS International Conference for Biomedical Robotics and Biomechatronics (BioRob). IEEE, 2024, pp. 1555–1560.

[23] O. Khatib, “A unified approach for motion and force control of robot manipulators: The operational space formulation,” *IEEE Journal on Robotics and Automation*, vol. 3, no. 1, pp. 43–53, 1987.

[24] M. Mistry and L. Righetti, “Operational space control of constrained and underactuated systems,” in *Robotics: Science and systems*, vol. 7, 2012, pp. 225–232.

[25] L. Righetti, J. Buchli, M. Mistry, and S. Schaal, “Inverse dynamics control of floating-base robots with external constraints: A unified view,” in 2011 IEEE international conference on robotics and automation. IEEE, 2011, pp. 1085–1090.

[26] F. Aghili and C.-Y. Su, “Control of constrained robots subject to unilateral contacts and friction cone constraints,” in 2016 IEEE international conference on robotics and automation (ICRA). IEEE, 2016, pp. 2347–2352.

[27] S. Wang, X. Chu, and K. S. Au, “Towards exact interaction force control for underactuated quadrupedal systems with orthogonal projection and quadratic programming,” in 2023 IEEE International Conference on Robotics and Automation (ICRA). IEEE, 2023, pp. 12 268–12 274.

[28] F. Aghili, “A unified approach for inverse and direct dynamics of constrained multibody systems based on linear projection operator: applications to control and simulation,” *IEEE Transactions on Robotics*, vol. 21, no. 5, pp. 834–849, 2005.

[29] J. Moura, V. Ivan, M. S. Erden, and S. Vijayakumar, “Equivalence of the projected forward dynamics and the dynamically consistent inverse solution,” in *Robotics: Science and Systems 2019*, 2019, pp. 1–10.

[30] A. De Luca, A. Albu-Schaffer, S. Haddadin, and G. Hirzinger, “Collision detection and safe reaction with the dlr-iii lightweight manipulator arm,” in 2006 IEEE/RSJ international conference on intelligent robots and systems. IEEE, 2006, pp. 1623–1630.

[31] C. Ott, *Cartesian impedance control of redundant and flexible-joint robots*. Springer, 2008.

[32] A. Dietrich, C. Ott, and S. Stramigioli, “Passivation of projection-based null space compliance control via energy tanks,” *IEEE Robotics and automation letters*, vol. 1, no. 1, pp. 184–191, 2015.

[33] H. Sadeghian, L. Villani, M. Keshmiri, and B. Siciliano, “Dynamic multi-priority control in redundant robotic systems1,” *Robotica*, vol. 31, no. 7, pp. 1155–1167, 2013.

[34] ———, “Task-space control of robot manipulators with null-space compliance,” *IEEE Transactions on Robotics*, vol. 30, no. 2, pp. 493–506, 2013.